Supplementary materials

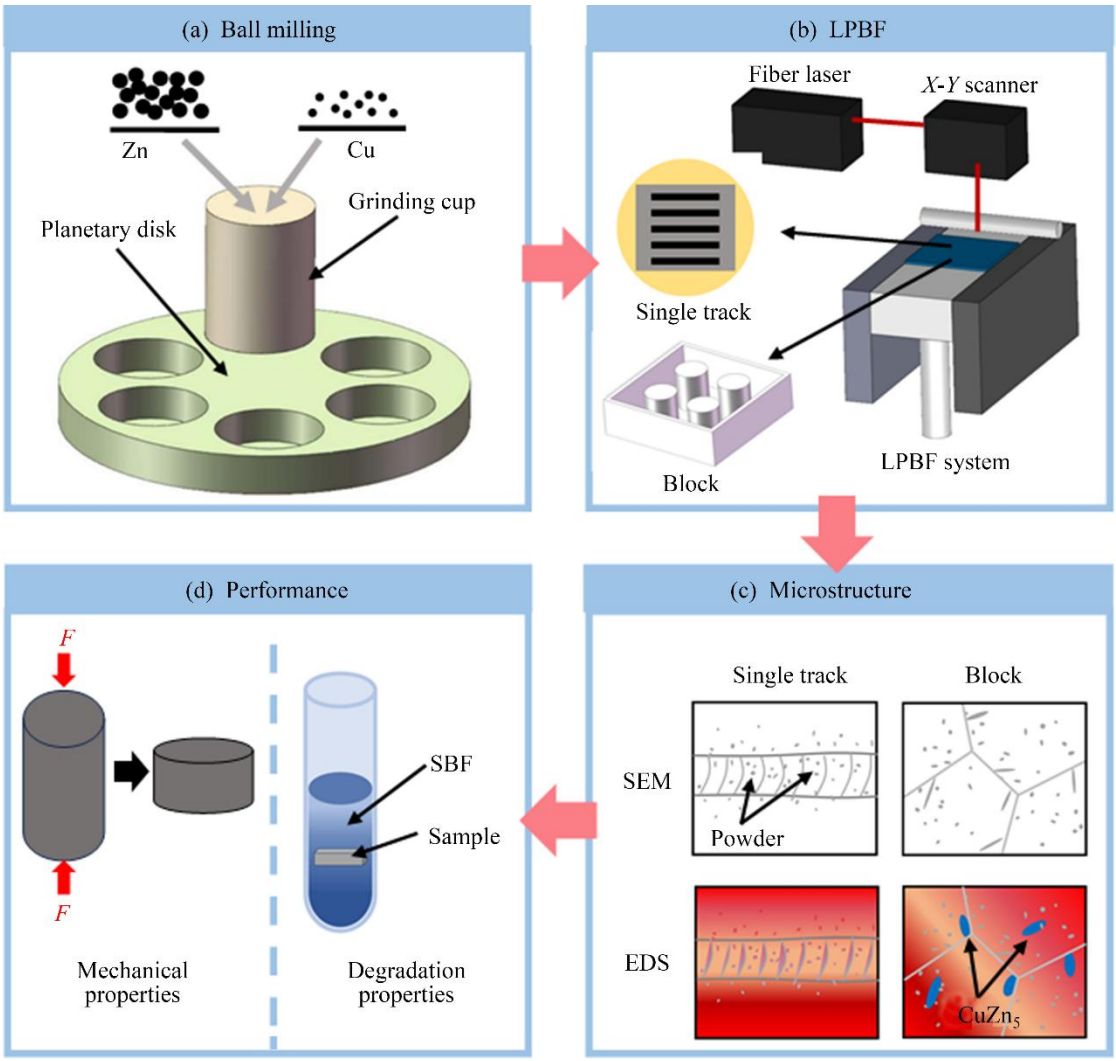

Figure S1 Schematic of the preparation process and characterization of Zn-4Cu alloys: (a) Ball milling; (b) LPBF; (c) Microstructure; (d) Performance

A 1.06 μm fiber laser beam was collimated through focusing lenses to form a 50 μm spot. Under argon shielding with real-time oxygen monitoring ($<10^{-6}$ O_2), the laser precisely melted Zn-4Cu alloy powder layers. Subsequent layers were deposited by a powder roller, enabling layer-by-layer fabrication of fully dense metallic components.

The LPBF single track experiments were carried out as following procedure: A Zn substrate was first ground and polished, followed by uniformly deposition of Zn-4Cu powder with a layer thickness of approximately 100 μm. Single tracks were then printed using the LPBF system under varying laser powers and scanning speeds. The LPBF block experiment process involved depositing powders layers on the prepared substrate, selectively scanning each layer with a laser beam to melt the powder and form a molten pool, which subsequently underwent rapid solidification, and repeating this layer-by-layer process to build three-dimensional structure.

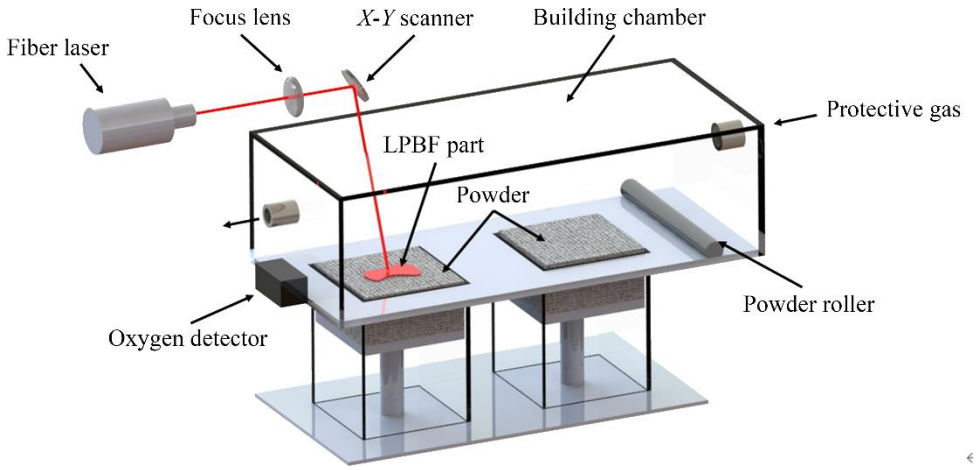

Figure S2 Detailed schematic of LPBF process

Specimens with cylindrical geometry compliant with ASTM E9-19 standard (φ(8.0±0.1) mm× (12.0±0.2) mm height) were tested under ambient conditions using a universal testing machine. Newly added images of as-built samples explicitly indicating build orientation (BD direction marked by black arrows) are presented in Figure S3.

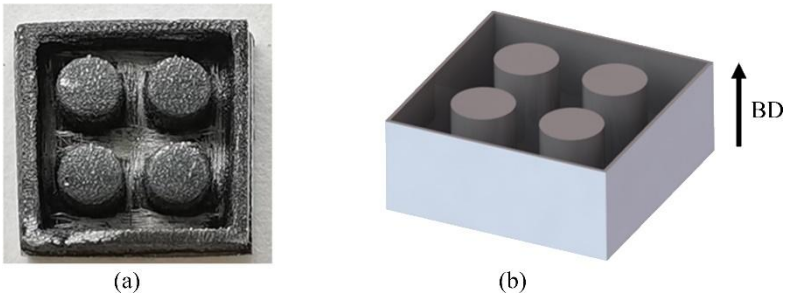

Figure S3 Images of built samples (a) and build orientation (b)

The hardness and compressive tests were conducted in accordance with the standard procedures of ASTM E384z respectively.

It can be further observed in Figure S4 that as scanning speed and laser power increased, there was an initial improvement followed by a subsequent deterioration in the uniformity and smoothness of the melting lines.

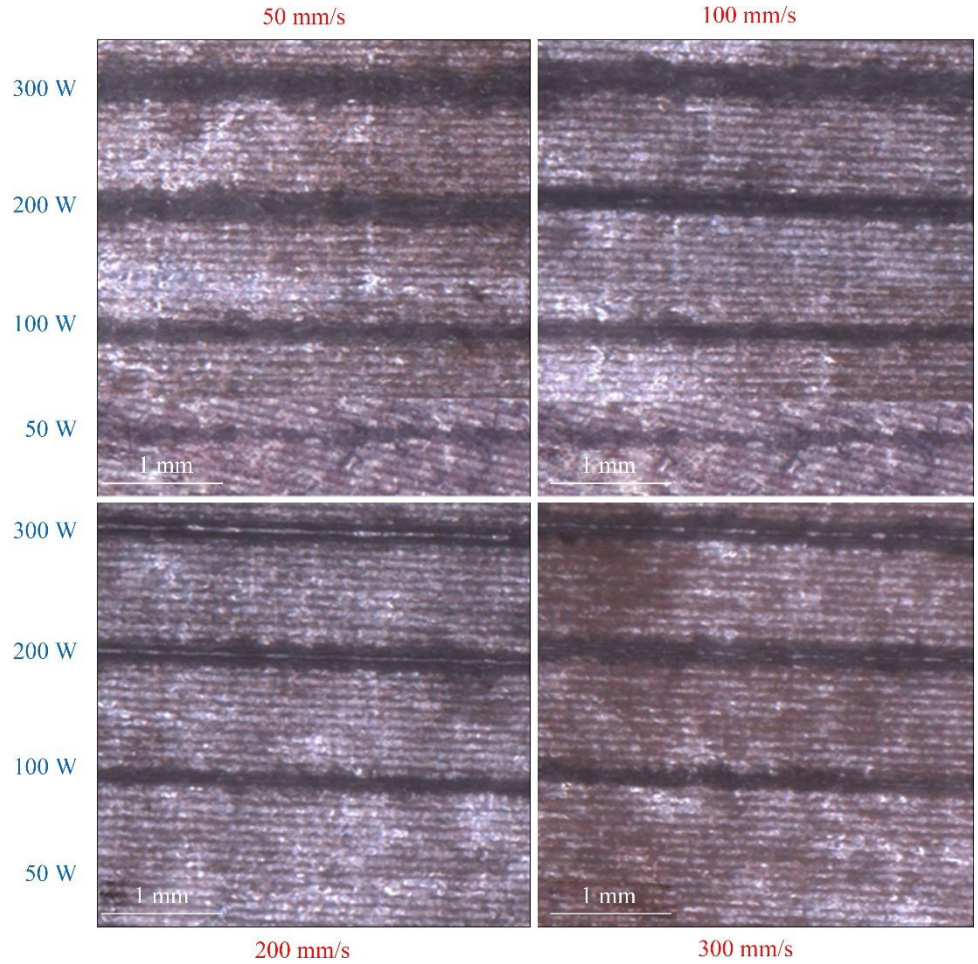

Figure S4 Surface topography of single tracks at different process parameters

After heat treatment, OM analysis revealed weakened boundaries of the $CuZn_5$ phase in the annealed samples (Figure S5(c)). SEM observations further confirmed that the size of the $CuZn_5$ phase in the heat-treated sample (Point 4) was reduced compared to that before heat treatment (Point 2) (Figure S5(e)). Additionally, EBSD image in Figure S5(c) indicated a marginal variation in average grain size from approximately 0.3 μm (Figure 7(c)) to 0.2 μm, and the kernel average misorientation (KAM) value decreased from 0.2430 to 0.1713. Meanwhile, the material hardness increased from 68.2HV to 73.3HV, whereas the yield strength slightly decreased from 160 to 152 MPa (Figure S5(a)). This can be attributed to grain refinement (Figure S6(b)), which enhances hardness by increasing grain boundary resistance to dislocation motion [1]. In addition, dislocation recovery and annihilation during annealing reduced the initial work-hardening capability [2], leading to the observed decline in strength.

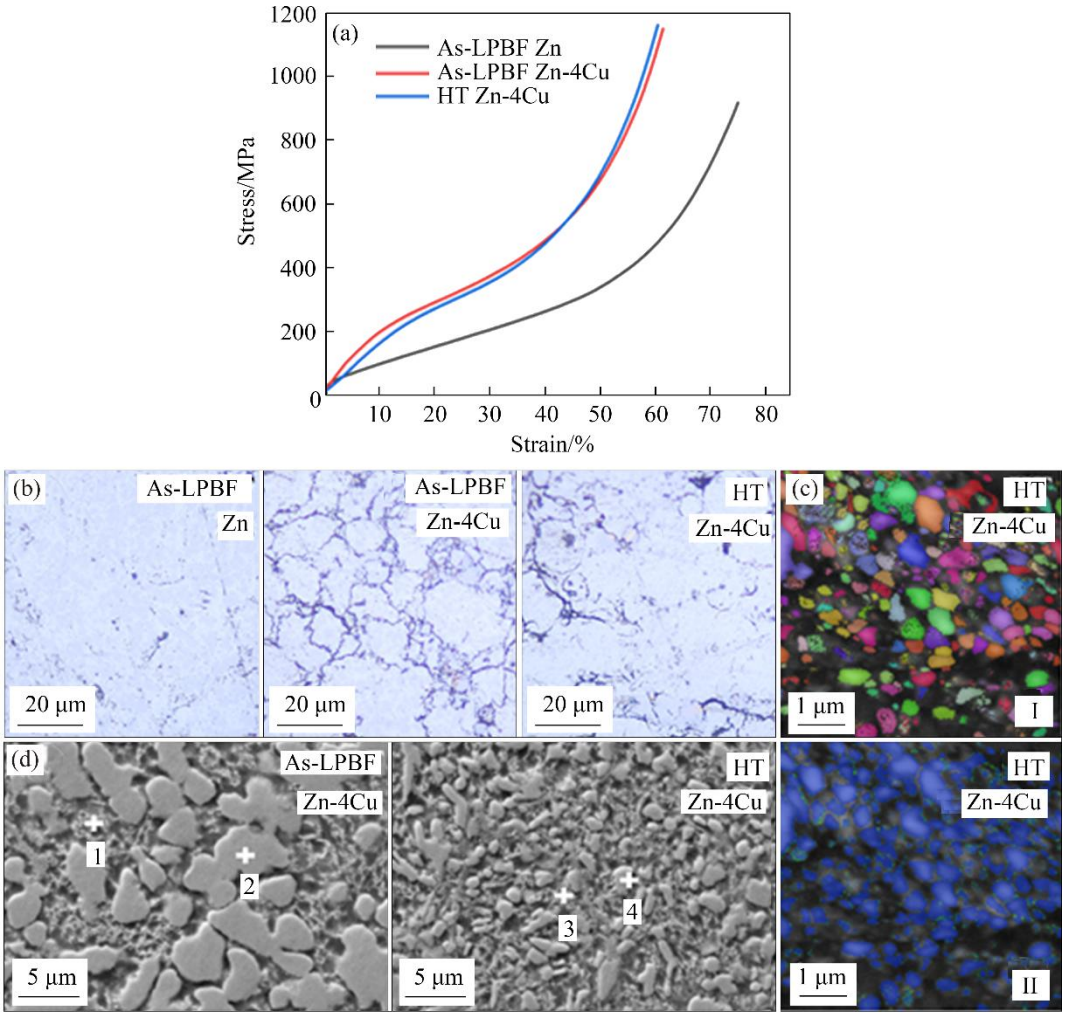

(e)

Element	Point 1	Point 2	Point 3	Point 4
w(Zn)/%	97.1	85.9	95.6	83.8
w(Cu)/%	2.9	14.1	4.4	16.2
w(Zn):*w*(Cu)	33.5	6.1	21.7	5.2

Figure S5 (a) Stress−strain curves, (b) OM images, (c) EBSD image (I) and KAM map (II), (d) SEM images and (e) EDS results of LPBFed and heat treated (HT) Zn-4Cu alloys, with LPBFed pristine Zn as control group

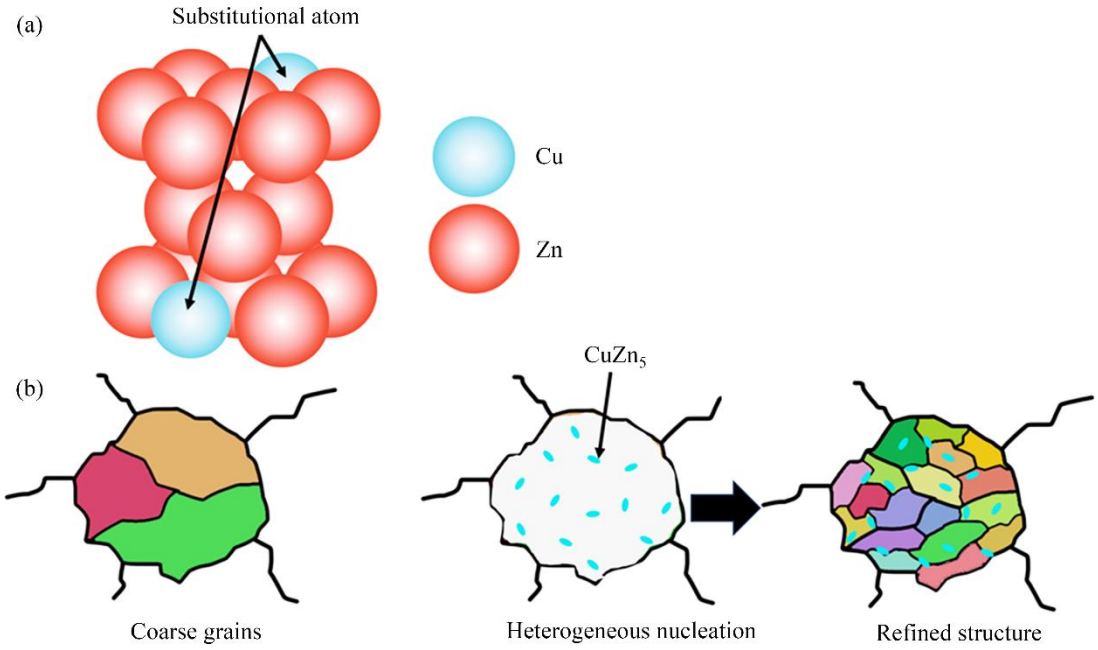

Figure S6 Schematic diagrams of strengthening mechanisms: (a) Solid solution strengthening; (b) Grain refinement

It can be seen that both the samples exhibited uniform degradation surfaces without localized degradation. The washing and drying process resulted in the partial removal of degradation products, thereby exposing the underlying substrate. Prior to their removal, the degradation layer of pristine Zn exhibited widespread coverage, featuring numerous discrete plates with visible cracks (Figure S7(a)). In contrast, the degradation layer of the Zn-4Cu alloys was denser, characterized by significantly smaller particle sizes and a flocculent distribution pattern (Figure S7(b)). The composition of degradation products comprised predominantly Zn, O, P, Ca, and a minor amount of Cu, indicating compounds such as ZnO, $Zn(OH)_2$, and Ca-P. Ca-P compounds are known as osteogenic precursors that promote cell adhesion and osteogenesis [3, 4]. After the removal of degradation products, the surfaces of both pristine Zn and Zn-4Cu alloys exhibited fine and uniformly distributed degradation pits, without noticeable cracks or localized corrosion (Figures S7(c) and (d)). The more homogeneous degradation behavior can be attributed to the fine and uniform grain structure attained through LPBF preparation. The presence of uniformly distributed secondary phases further contributed to the uniform degradation [5]. This uniform corrosion mode prevents stress concentration and maintains mechanical integrity during service, which is critical for the long-term stability of load-bearing bone implants.

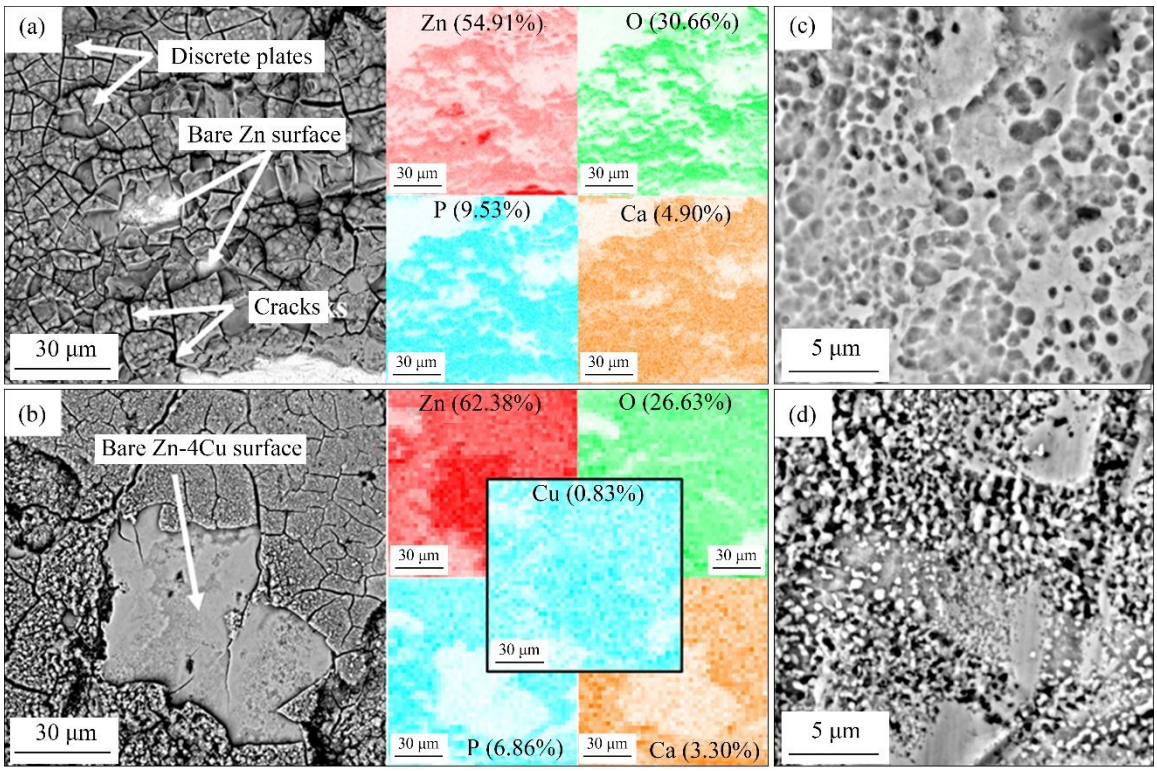

Figure S7 Degradation morphology and corresponding EDS mapping of (a) Zn and (b) Zn-4Cu alloys after immersion tests; Surface morphology of (c) Zn and (d) Zn-4Cu alloys after removing degradation products

The accelerated degradation is attributable to three concurrent mechanisms: 1) Formation of benign micro-galvanic couples between $CuZn_5$ phases (cathode with moderately higher potential) and Zn matrix (local anode), promoting uniform micro-dissolution; 2) EBSD quantification confirmed a 3.16-fold increase in grain boundary density (Figure 5(c)), accelerating atomic diffusion and corrosion media penetration [6]; 3) Higher relative density (>99.5%) of LPBF-processed Zn-4Cu alloy versus pristine Zn, coupled with homogeneous dispersion of $CuZn_5$ phases (Figure 5(a)), eliminates localized corrosion channels [7]. Collectively, these mechanisms yield uniformly distributed micro-pits (Figure S7(d)) instead of localized pitting or crack propagation, significantly reducing the risk of premature implant fracture. Furthermore, the degradation rate of the LPBFed Zn-4Cu alloy increased from 0.16 to 0.18 mm/year after vacuum annealing. This might be attributed to grain refinement (Figure S5(c)) and the resulting increase in grain boundary area, which facilitated the penetration and reaction of the corrosive medium at grain boundaries [8].

In the future, Zn-based alloys may be combined with bioactive ceramics or other biodegradable metals (such as Mg or Fe) to achieve a better balance between mechanical performance and biological functionality. The optimization of post-processing heat treatments could further refine precipitates morphology, grain size, and residual stress states, thereby enhancing the overall mechanical properties and long-term stability of the alloys. Additionally, in vivo degradation and biocompatibility evaluations are essential to determine whether the degradation rates and micro-corrosion mechanisms observed under in vitro conditions remain consistent in physiological environments, ultimately facilitating the clinical translation of Zn-Cu alloys for implant applications.

References

[1] CAI Han-yu, PENG Jia-xin, ZHOU Yu-xi, et al. Microstructure and properties of high strength and high conductivity Cu-0.48Cr-0.20Nb-0.27Zn alloy treated by a new combined thermo-mechanical treatment [J]. Materials Science and Engineering A, 2023, 888: 145802. DOI: 10.1016/j.msea.2023.145802.

[2] ZHANG Yan-min, HUANG Bao-huan, GAO Hong-jiao, et al. Effect of annealing time on bending performance and microstructure of

C19400 alloy strip [J]. Nanotechnology Reviews, 2024, 13: 20240075. DOI: 10.1515/ntrev-2024-0075.
[3] YANG Wen-jing, JI Yi-bing, LI Lang, et al. Persistent glutathione-depleting MFO@MIL nanoreactors enhance the antitumor efficiency of a skin scaffold [J]. Materials Chemistry Frontiers, 2025, 9(8): 1249−1258.
[4] SHUAI Ci-jun, PAN Gao, WANG Zheng, et al. Bifunctional MoS_2@Cu_2O heterojunction within scaffold for dual-mode synergistic antibacterial effects [J]. Applied Surface Science, 2025, 686: 162154. DOI: 10.1016/j.apsusc.2024.162154.
[5] YUE Rui, ZHANG Jian, KE Gui-zhou, et al. Effects of extrusion temperature on microstructure, mechanical properties and in vitro degradation behavior of biodegradable Zn-3Cu-0.5Fe alloy [J]. Materials Science and Engineering C, 2019, 105: 110106. DOI: 10.1016/j.msec.2019.110106.
[6] WANG Yu-jiao, ZHANG Yun, JIANG Hai-tao. Effect of grain size uniformity and crystallographic orientation on the corrosion behavior of Mg-2Zn-1Al bar [J]. Materials Characterization, 2021, 179: 111374. DOI: 10.1016/j.matchar.2021.111374.
[7] LIU Jing-bo, WANG De-kuan, LIU Bo, et al. Microstructural evolution, mechanical properties and corrosion mechanisms of additively manufactured biodegradable Zn-Cu alloys [J]. Journal of Materials Science & Technology, 2024, 186: 142−157. DOI: 10.1016/j.jmst.2023.10.052.
[8] SOLEIMANI M, MIRZADEH H, DEHGHANIAN C. Effect of grain size on the corrosion resistance of low carbon steel [J]. Materials Research Express, 2020, 7(1): 016522. DOI: 10.1088/2053-1591/ab62fa.